Journal of Scientific Computing (2020) 82:43
https://doi.org/10.1007/s10915-020-01135-x

An h—Adaptive Local Discontinuous Galerkin Method for Simulating Wormhole Propagation with Darcy–Forcheiner Model

Lulu Tian[1] · Hui Guo[1] · Rui Jia[1] · Yang Yang[2]

Received: 19 December 2019 / Revised: 13 January 2020 / Accepted: 18 January 2020 /
Published online: 10 February 2020

Abstract
In this paper, we apply local discontinuous Galerkin methods to the compressible wormhole propagation. With high velocity, Darcy–Forchheimer model is used instead of classical Darcy framework. Optimal error estimates for the pressure, velocity, porosity and concentration in different norms are established on non-uniform rectanglular grids. To capture the propagation of the wormhole accurately and save computations, adaptive mesh is applied. Numerical experiments are presented to verify the theoretical analysis and show the good performance of the LDG scheme for compressible wormhole propagation.

Keywords Local discontinuous Galerkin method · Error estimate · Compressible wormhole propagation · Adaptive mesh

Mathematics Subject Classification 65M15 · 65M60

Lulu Tian was supported by National Natural Science Foundation of China 11801569 and Natural Science Foundation of Shandong Province (CN) ZR2018BA011. The second author was supported by National Natural Science Foundation of China Grants 11571367 and the Fundamental Research Funds for the Central Universities 18CX05003A. The last author was supported by NSF Grant DMS-1818467. This work is also supported by the National Natural Science Foundation of China (41974133).

✉ Hui Guo
sdugh@163.com

Lulu Tian
Tianll@upc.edu.cn

Rui Jia
UPCJiaRui@163.com

Yang Yang
yyang7@mtu.edu

[1] College of Science, China University of Petroleum, Qingdao 266580, China

[2] Michigan Technological University, Houghton, MI 49931, USA

1 Introduction

Acid treatment of carbonate reservoirs plays an important role in increasing the permeability of the damaged zone near the wells. The injected acid can dissolve the material near the well, hence establishes a channel connecting the reservoir and the well, gaining the production rate. However, given the amount of acid, the relative increase in permeability is strongly related to the injection conditions, and the long conductive channels, namely wormholes, cannot be formed unless suitable flow rates have been reached. With the formation of the wormholes, the channels can penetrate deep into the material and facilitate the flow of oil. Thus, for successful stimulation of a well it is required to produce wormholes with optimum density and penetrating deep into the formation.

The wormhole propagation has been analyzed mathematically by many authors [14,16, 26,33,40,41]. However, quite few works focusing on the numerical simulations. In [58], the chemical-dissolution front instability were discussed theoretically and numerically. Subsequently, the parallel simulation was investigated in [49]. Later, in [23], the authors applied the mixed finite element method and studied the stability and error estimates for velocity, pressure, concentration and porosity under different norms. Moreover, in [24] the second-order block-centered finite difference method has been constructed. Recently, high-order local discontinuous Galerkin (LDG) methods were also applied to wormhole propagation [17]. Besides the above, the bound-preserving technique for the incompressible problem was investigated in [53], following the idea introduced in [6,18]. All the works given above except [23] considered Darcy flow only. However, it may not yield correct solutions if the velocity of the fluid is high, especially in the high-porosity area. In [38], The Darcy–Forchheiner model has been proposed that could yield more reasonable results. Numerical methods for Darcy–Forchheiner model have been investigated by many authors [27,32,36,37,50,59]. In addition, in [31], the authors coupled miscible displacements with the Darcy–Forchheiner model. To the best knowledge, no previous works focusing on discontinuous Galerkin methods for Darcy–Forchheiner model coupled with wormhole propagation.

The DG method was first introduced in 1973 by Reed and Hill [35] in the framework of neutron linear transport. Subsequently, Cockburn et al. developed Runge–Kutta discontinuous Galerkin (RKDG) methods for hyperbolic conservation laws in a series of papers [8–11]. Motivated by Bassi and Rebay [2], in [12], Cockburn and Shu first introduced the LDG method to solve the convection–diffusion equation. In LDG methods, several auxiliary variables, approximating the gradient of the solution, have to be introduced to form a first-order system, representing the original equation with high-order derivatives. Then it is possible to apply the DG method to each equation in the new system. With suitable numerical fluxes, the stability and optimal error estimates can be obtained [51,52,54,55]. Moreover, those auxiliary variables can be solved locally. Therefore, the LDG methods share the same advantages of the DG methods, such as good stability, high order accuracy, flexibility on h-p adaptivity and on complex geometry.

The LDG methods would be suitable for most of the convection–diffusion equations. However, if the coefficient of the convection term contains other variables or their derivatives, the error estimates may not be easy to obtain. It is well known that for hyperbolic equations with discontinuous coefficients, the existence and uniqueness of the solutions may not be valid [15,21]. After the spatial discretization, due to the inter-element discontinuities of two independent solution variables, the convection term turns out to be discontinuous across the cell interfaces. Therefore, it is difficult to obtain the error estimates if we analyze the convection and diffusion terms separately. Recently, Wang et al. [46–48] applied IMEX

time integration and obtained optimal error estimates of the LDG methods for convection–diffusion problems. Subsequently, the idea has been applied to miscible displacements in porous media [19,20,57], chemotaxis model [25] to obtain optimal rates of convergence. The basic idea for the new technique is to extract an important relationship between the solution polynomial for the auxiliary variable of the gradient of the primitive variable and the gradient of the numerical approximation of the primitive variable, see Lemma 4.4. Due to the usage of the Darcy–Forchheiner model, we need to introduce more auxiliary variables to take the advantages of the new technique provided in [46–48]. Moreover, the systems are coupled together. To obtain the optimal error estimates, we will derive four energy inequalities. In this paper, we will obtain the estimates in $L^\infty(0, T; L^2)$ for concentration c, in $L^2(0, T; L^2)$ for $\mathbf{s} = -\nabla c$, in $L^\infty(0, T; L^2)$ for porosity ϕ and in $L^\infty(0, T; L^2)$ for pressure p. Moreover, different from most of the previous work [17], we do not assume the effective dispersion tensor $\mathbf{D}$ to be a diagonal matrix.

In order to simulate wormholes propagations and to reduce the computational cost we consider adaptive meshes. To start the mesh adaptation, we first need a criterion to decide whether an element in the computational mesh needs to be refined or coarsened. Two main types of criteria for refinement and coarsening are used in finite volume and finite element methods: error estimators and heuristic indicators. Error estimators are based on theoretical results, and they are only available when a posteriori error estimates hold. For example, a posteriori error estimates can be found for finite volume schemes for scalar and nonlinear hyperbolic systems of conservation laws [1,22,29,30,43,44]. Heuristic indicators usually depend on local gradients of thermodynamic variables such as density, pressure, energy and entropy. Compared with a posteriori error estimates, heuristic indicators are easy to compute, and are widely used in practical applications [3,4,13,45], but they have a limited theoretical foundation. Several indicators for adaptive Runge–Kutta discontinuous Galerkin methods for hyperbolic conservation laws can be found in [34,60,61]. Recently, an h-adaptive LDG methods are applied for the Navier–Stokes–Korteweg equations using gradient of the density as an indicator [42]. Since a reliable a posteriori error estimate is currently out of scope for LDG discretizations of the equations modeling wormhole propagations, a heuristic indicator is chosen in this article, which is based on the jump of the porosity and concentration.

The paper is organized as follows. In Sect. 2, we demonstrate the governing equations of the compressible wormhole propagation coupled with Darcy–Forchheiner model. In Sect. 3, we present some preliminaries, including the basic notations and norms to be used throughout the paper and the LDG spatial discretization. Section 4 is the main body of the paper where we present the projections and some essential properties of the finite element spaces, error equations and the details of the optimal error estimates for compressible wormhole propagation. We provide mesh adaptation in Sect. 5 to save computational costs in two dimensional practical simulations. Numerical results are given to demonstrate the accuracy and capability of the method in Sect. 6. We will end in Sect. 7 with some concluding remarks.

2 Compressible Wormhole Propagation

Consider a rectangle domain $\Omega = [0, 1] \times [0, 1]$ in R^2. The model of the compressible wormhole propagation couple with Darcy–Forchheiner flow in two space dimensions are given by [17,23,24]:

$$\gamma \frac{\partial p}{\partial t} + \frac{\partial \phi}{\partial t} + \nabla \cdot \mathbf{u} = f, \tag{2.1}$$

$$\frac{\rho}{\phi}\frac{\partial \mathbf{u}}{\partial t} + \frac{\mu}{\kappa(\phi)}\mathbf{u} + \frac{\rho F}{\sqrt{\kappa(\phi)}}|\mathbf{u}|\,\mathbf{u} = -\nabla p + \rho \mathbf{g}, \tag{2.2}$$

$$\frac{\partial(\phi c_f)}{\partial t} + \nabla \cdot (\mathbf{u} c_f) = \nabla \cdot (\phi \mathbf{D}(\mathbf{u}) \nabla c_f) + k_c a_v (c_s - c_f) + f_p c_f + f_I c_I, \tag{2.3}$$

$$\frac{\partial \phi}{\partial t} = \frac{\alpha k_c a_v (c_f - c_s)}{\rho_s}, \tag{2.4}$$

$(x, y) \in \Omega, 0 < t \leq T$, where p is the pressure in the fluid mixture, $\mathbf{u}$ is the Darcy velocity of the mixture, ϕ is the porosity of the rock, and c_f is the cup-mixing concentration of the acid in the fluid phase. ρ and $\mathbf{g}$ are the mass density and the gravity vector, respectively. μ is the viscosity and γ is a pseudo-compressibility parameter that results in slight change of the density of the fluid phase in the dissolution process. $F = \frac{1.75}{\sqrt{150\phi^3}}$ is porcheimer number. $f = f_I + f_p$ is the external volumetric flow rate with f_p and f_I being the production and injection rates, respectively. c_I is the injected concentration. The effective dispersion tensor $\mathbf{D}(\mathbf{u})$ is defined as

$$\mathbf{D}(\mathbf{u}) = d_m \mathbf{I} + |\mathbf{u}| \left(\alpha_l \mathbf{E}(\mathbf{u}) + \alpha_t (\mathbf{I} - \mathbf{E}(\mathbf{u}))\right), \tag{2.5}$$

where

$$(\mathbf{E}(\mathbf{u}))_{ij} = \frac{u_i u_j}{|\mathbf{u}|^2}, \quad 1 \leq i, j \leq 2.$$

In (2.5), d_m is the molecular diffusivity that is assumed to be strictly positive; α_l and α_t are the longitudinal and the transverse dispersivities, respectively, and both of them are assumed to be positive. The variable c_s is the concentration of the acid at the fluid-solid interface given as

$$c_s = \frac{c_f}{1 + k_s/k_c}, \tag{2.6}$$

where k_c is the local mass-transfer coefficient and k_s is the surface reaction rate constant. κ in the second term on the left hand side of (2.2) is the permeability of the rocks. The permeability has a relationship with the porosity, given by the Carman–Kozeny correlation [28]

$$\frac{\kappa}{\kappa_0} = \frac{\phi}{\phi_0}\left(\frac{\phi(1-\phi_0)}{\phi_0(1-\phi)}\right)^2, \tag{2.7}$$

where ϕ_0 and κ_0 are the initial porosity and permeability of the rock, respectively. Then we consider κ as a function of ϕ, and the following equation holds

$$\frac{1}{\kappa(\phi)} = \kappa^{-1}(\phi) = \frac{\phi_0}{\phi \kappa_0}\left(\frac{\phi_0(1-\phi)}{\phi(1-\phi_0)}\right)^2.$$

In (2.4), α is the dissolving power of the acid and ρ_s is the density of the solid phase. a_v is the interfacial area available for reaction per unit volume of the medium. Using porosity and permeability, a_v is shown as

$$\frac{a_v}{a_0} = \frac{\phi}{\phi_0}\sqrt{\frac{\kappa_0 \phi}{\kappa \phi_0}} = \frac{1-\phi}{1-\phi_0}, \tag{2.8}$$

where a_0 is the initial interfacial area. The initial conditions are given as

$$c_f(x, y, 0) = c_0(x, y), \quad p(x, y, 0) = p_0(x, y), \quad \phi(x, y, 0) = \phi_0(x, y), \quad \mathbf{u}(x, y, 0) = \mathbf{u}_0(x, y).$$

For simplicity, we consider periodic boundary condition in this paper. The analysis for homogeneous Neumann boundary can be obtained following the same lines with some minor changes, and we thus omit it.

Finally, we make the following hypotheses (H) for the problem.

1. $0 < \phi_* \le \phi(x, y) \le \phi^* < 1$.
2. $\mathbf{D}(\mathbf{u})$ is uniformly Lipschtiz continuous, and for any $\mathbf{v}$, $\mathbf{w} \in R^2$ there exist two positive constants D_*, D^* such that $\mathbf{v}^T\mathbf{D}\mathbf{v} \ge D_*\mathbf{v}^T\mathbf{v} = D_*\|\mathbf{v}\|^2$ and $\mathbf{v}^T\mathbf{D}\mathbf{w} \le D^*\|\mathbf{v}\|\|\mathbf{w}\|$, where $\|\mathbf{v}\|$ is the standard Euclidian norm in R^2.
3. $\gamma, \alpha, \rho_s, \mu, k_c$, and k_s are all given positive constants, and $0 < \phi_{0*} \le \phi_0 \le \phi_0^* < 1$, $0 < a_{0*} \le a_0 \le a_0^*$.
4. $c_f, \phi, c_{f_t}, \phi_t, \mathbf{u}$ and $\mathbf{s} = -\nabla c_f$ are uniformly bounded in $R^2 \times [0, T]$.

It is easy to obtain the following lemma.

Lemma 2.1 *Suppose hypotheses 1 and 3 are satisfied, then $a_v(\phi)$, $\kappa^{-1}(\phi)$ and $F(\phi)$ are bounded and Lipschitz continuous, i.e. there exists C such that*

$$\begin{aligned}
&a_v(\phi) \le C, \quad C_* \le \kappa^{-1}(\phi) \le C^*, \quad F(\phi) \le C,\\
&|a_v(\phi_1) - a_v(\phi_2)| \le C|\phi_1 - \phi_2|, \quad |\kappa^{-1}(\phi_1) - \kappa^{-1}(\phi_2)| \le C|\phi_1 - \phi_2|,\\
&|F(\phi_1) - F(\phi_2)| \le C|\phi_1 - \phi_2|.
\end{aligned}$$

3 Preliminaries

In this section, we will demonstrate some preliminary results that will be used throughout the paper.

3.1 Basic Notations

We denote by Ω_h a tessellation of Ω with regular rectangle elements K. We assume the partition is quasi-uniform, i.e. $h = min_{K\in\Omega_h} diam(K)$, with diam$(K)$ the longest edge of element K. The finite element space is chosen as

$$W_h^k = \{z : z|_K \in Q^k(K), \forall K \in \Omega_h\},$$

where $Q^k(K)$ denotes the space of tensor product polynomials of degrees at most k in K. We denote Γ_h to be the set of all element interfaces and $\Gamma_0 = \Gamma_h \backslash \partial\Omega$. Let $\mathcal{E} \in \Gamma_0$ be an interior edge shared by the "left" and "right" elements K_ℓ and K_r if $\mathcal{E}$ is vertical, or "bottom" and "top" if $\mathcal{E}$ is horizontal. The normal vectors $\mathbf{n}_\ell$ and $\mathbf{n}_r$ on $\mathcal{E}$ being the outward normals of K_ℓ and K_r, respectively. For any $z \in W_h^k$, we define $z^- = z|_{\partial K_\ell}$ and $z^+ = z|_{\partial K_r}$, respectively. The jump is given as $[z] = z^+ - z^-$. Moreover, for $\mathbf{s} \in \mathbf{W}_h^k = W_h^k \times W_h^k$, we define $\mathbf{s}^+$ and $\mathbf{s}^-$ and $[\mathbf{s}]$ analogously. For more details about these definitions, we refer the reader to [17].

Throughout this paper, the symbol C is used as a generic constant which may appear differently at different occurrences. Moreover, the symbol ϵ is a sufficiently small positive constant.

3.2 Norms

In this subsection, we define several norms that will be used throughout the paper.

Denote $\|u\|_{0,K}$ to be the standard L^2-norm of u in cell K. For any natural number ℓ, we consider the norm of the Sobolev space $H^\ell(K)$, defined by

$$\|u\|_{\ell,K} = \left\{ \sum_{0\le\alpha+\beta\le\ell} \left\| \frac{\partial^{\alpha+\beta} u}{\partial x^\alpha \partial y^\beta} \right\|_{0,K}^2 \right\}^{\frac{1}{2}}.$$

Moreover, we define the norms on the whole computational domain as

$$\|u\|_\ell = \left(\sum_{K\in\Omega_h} \|u\|_{\ell,K}^2 \right)^{\frac{1}{2}}.$$

For convenience, if we consider the standard L^2-norm, then the corresponding subscript will be omitted.

Let Γ_K be the edges of K, and we define

$$\|u\|_{\Gamma_K}^2 = \int_{\partial K} u^2 ds.$$

We also define

$$\|u\|_{\Gamma_h}^2 = \sum_{K\in\Omega_h} \|u\|_{\Gamma_K}^2.$$

Moreover, we define the standard L^∞ norm of u in K as $\|u\|_{\infty,K}$, and define the L^∞ norm on the whole computational domain as

$$\|u\|_\infty = \max_{K\in\Omega_h} \|u\|_{\infty,K}.$$

Definitions of the norms for vector $\mathbf{u} = (u_1, u_2)^T$ are analogy. More details can be found in [17].

3.3 LDG Scheme

In this section, we propose an LDG discretization for modelling equations of wormhole propagation (2.6)–(2.8), which can be rewritten as a first order system,

$$\gamma \frac{\partial p}{\partial t} + \frac{\partial \phi}{\partial t} + \nabla\cdot\mathbf{u} = f, \tag{3.1}$$

$$\frac{\rho}{\phi}\frac{\partial \mathbf{u}}{\partial t} + \frac{\mu}{\kappa(\phi)}\mathbf{u} + \frac{\rho F}{\sqrt{\kappa(\phi)}}|\mathbf{u}|\,\mathbf{u} = -\nabla p + \rho\mathbf{g}, \tag{3.2}$$

$$\frac{\partial(\phi c_f)}{\partial t} + \nabla\cdot(\mathbf{u}c_f) + \nabla\cdot\mathbf{z} + Aa_v(\phi)c_f = f_p c_f + f_I c_I, \tag{3.3}$$

$$\mathbf{s} = -\nabla c_f, \tag{3.4}$$

$$\mathbf{z} = \phi\mathbf{D}(\mathbf{u})\mathbf{s}, \tag{3.5}$$

$$\frac{\partial \phi}{\partial t} = Ba_v(\phi)c_f. \tag{3.6}$$

where $A = \frac{k_c k_s}{k_c+k_s}$, $B = \frac{\alpha k_c k_s}{\rho_s(k_c+k_s)}$ and $a_v(\phi) = \frac{a_0(1-\phi)}{1-\phi_0}$. The LDG discretization for the wormhole propagation equations (3.1)–(3.6) is now as follows: find $c_h, p_h, \phi_h \in W_h^k$ and $\mathbf{u}_h, \mathbf{s}_h, \mathbf{z}_h \in \mathbf{W}_h^k$, such that for all test functions $\zeta, v, \beta \in W_h^k, \boldsymbol{\theta}, \mathbf{w}, \boldsymbol{\psi} \in \mathbf{W}_h^k$, the following relations are satisfied

$$\left(\gamma \frac{\partial p_h}{\partial t}, \zeta\right)_K + \left(\frac{\partial \phi_h}{\partial t}, \zeta\right)_K = \mathcal{L}_K^d(\mathbf{u}_h, \zeta) + (f, \zeta)_K \tag{3.7}$$

$$\left(\frac{\rho}{\phi_h}\frac{\partial \mathbf{u_h}}{\partial t}, \boldsymbol{\theta}\right)_K + \left(\frac{\mu}{\kappa(\phi_h)}\mathbf{u}_h, \boldsymbol{\theta}\right)_K + \left(\frac{\rho F(\phi_h)}{\sqrt{\kappa(\phi_h)}}|\mathbf{u}_h|\,\mathbf{u}_h, \boldsymbol{\theta}\right)_K = \mathcal{D}_K(p_h, \boldsymbol{\theta}) + (\rho \mathbf{g}, \boldsymbol{\theta})_{\mathbf{K}} \tag{3.8}$$

$$((\phi_h c_h)_t, v)_K = \mathcal{L}_K^c(\mathbf{u}_h, c_h, v) + \mathcal{L}_K^d(\mathbf{z}_h, v) + (f_p c_h + f_I c_I, v)_K - (A a_v(\phi_h) c_h, v)_K \tag{3.9}$$

$$(\mathbf{s}_h, \mathbf{w})_K = \mathcal{D}_K(c_h, \mathbf{w}) \tag{3.10}$$

$$(\mathbf{z}_h, \boldsymbol{\psi})_K = (\phi_h \mathbf{D}(\mathbf{u}_h)\mathbf{s}_h, \boldsymbol{\psi})_K \tag{3.11}$$

$$(\phi_{ht}, \beta)_K = (B a_v(\phi_h) c_h, \beta)_K \tag{3.12}$$

where

$$\begin{aligned}
\mathcal{L}_K^c(\mathbf{s}, c, v) &= (\mathbf{s}c, \nabla v)_K - \langle \widehat{\mathbf{s}c} \cdot \boldsymbol{\nu}_K, v\rangle_{\partial K},\\
\mathcal{L}_K^d(\mathbf{s}, v) &= (\mathbf{s}, \nabla v)_K - \langle \widehat{\mathbf{s}} \cdot \boldsymbol{\nu}_K, v\rangle_{\partial K},\\
\mathcal{D}_K(c, \mathbf{w}) &= (c, \nabla \cdot \mathbf{w})_K - \langle \widehat{c}, \mathbf{w} \cdot \boldsymbol{\nu}_K\rangle_{\partial K},
\end{aligned}$$

and $(u, v)_K = \int_K uv dxdy$, $(\mathbf{u}, \mathbf{v})_K = \int_K \mathbf{u} \cdot \mathbf{v} dxdy$, $\langle u, v\rangle_{\partial K} = \int_{\partial K} uv ds$ and $\boldsymbol{\nu}_K$ is the outer unit normal of K. Alternating fluxes are chosen for the diffusion term, given by

$$\widehat{\mathbf{z}_h} = \mathbf{z}_h^-, \quad \widehat{c_h} = c_h^+, \quad \widehat{\mathbf{u}_h} = \mathbf{u}_h^-, \quad \widehat{p_h} = p_h^+.$$

We take Lax–Friedrich flux for the convection term,

$$\widehat{\mathbf{u}_h c_h} = \frac{1}{2}(\mathbf{u}_h^+ c_h^+ + \mathbf{u}_h^- c_h^- - \alpha \boldsymbol{\nu}_e (c_h^+ - c_h^-)),$$

where $\alpha \geq 0$ can be chosen as any fixed constant independent of h and $\boldsymbol{\nu}_e$ is the unit normal of $e \in \Gamma_0$ such that $(1, 1) \cdot \boldsymbol{\nu}_e > 0$.

Lemma 3.1 *We choose the initial solution as*

$$c_h(x, y, 0) = P^+ c_0, \quad \phi_h(x, y, 0) = P_k \phi_0, \quad p_h(x, y, 0) = P^+ p_0, \quad \mathbf{u}_h(x, y, 0) = \Pi^- \mathbf{u}_0. \tag{3.13}$$

then we have

$$\begin{aligned}
&\|c_f(x, y, 0) - c_h(x, y, 0)\| \leq C h^{k+1}, \quad \|p(x, y, 0) - p_h(x, y, 0)\| \leq C h^{k+1},\\
&\|\phi(x, y, 0) - \phi_h(x, y, 0)\| \leq C h^{k+1}, \quad \|\mathbf{u}(x, y, 0) - \mathbf{u}_h(x, y, 0)\| \leq C h^{k+1}.
\end{aligned}$$

3.4 The Main Theorem

We will use several special projections in this paper. Firstly, we define P^+ into W_h^k which is, for each cell K

$$
\begin{aligned}
&(P^+u-u,v)_K=0,\quad \forall v\in Q^{k-1}(K),\\
&\int_{J_j}(P^+u-u)\left(x_{i-\frac{1}{2}},y\right)v(y)dy=0,\quad \forall v\in P^{k-1}(J_j),\\
&\int_{I_i}(P^+u-u)\left(x,y_{j-\frac{1}{2}}\right)v(x)dx=0,\quad \forall v\in P^{k-1}(I_i),\\
&(P^+u-u)\left(x_{i-\frac{1}{2}},y_{j-\frac{1}{2}}\right)=0,
\end{aligned}
$$

where P^k denotes the polynomials of degree k. Moreover, we also define Π_x^- and Π_y^- into W_h^k which are, for each cell K,

$$
\begin{aligned}
&(\Pi_x^-u-u,v_x)_K=0,\quad \forall v\in Q^k(K),\\
&\int_{J_j}(\Pi_x^-u-u)\left(x_{i+\frac{1}{2}},y\right)v(y)dy=0,\quad \forall v\in P^k(J_j),\\
&(\Pi_y^-u-u,v_y)_K=0,\quad \forall v\in Q^k(K),\\
&\int_{I_i}(\Pi_y^-u-u)\left(x,y_{j+\frac{1}{2}}\right)v(x)dx=0,\quad \forall v\in P^k(I_i),
\end{aligned}
$$

as well as a vectored-valued projection $\Pi^-=\Pi_x^-\otimes\Pi_y^-$. Finally, we also use the L^2-projection P_k into W_h^k which is, for each cell K

$$
(P_ku-u,v)_K=0,\quad \forall v\in Q^k(K), \tag{3.14}
$$

and its two dimensional version $\mathbf{P}_k=P_k\otimes P_k$. For the special projections given above, we will demonstrate the following lemma by the standard approximation theory [7].

We define

$$
(u,v)=\sum_{K\in\Omega_h}(u,v)_K,\quad (\mathbf{u},\mathbf{v})=\sum_{K\in\Omega_h}(\mathbf{u},\mathbf{v})_K,
$$

and

$$
\begin{aligned}
\mathcal{L}^c(\mathbf{s},c,v)&=\sum_{K\in\Omega_h}\mathcal{L}_K^c(\mathbf{s},c,v),\\
\mathcal{L}^d(\mathbf{s},v)&=\sum_{K\in\Omega_h}\mathcal{L}_K^d(\mathbf{s},v),\\
\mathcal{D}(c,\mathbf{w})&=\sum_{K\in\Omega_h}\mathcal{D}_K(c,\mathbf{w}).
\end{aligned}
$$

It is easy to check the following identity by integration by parts on each cell.

Lemma 3.2 *For any functions v and $\mathbf{w}$,*

$$
\mathcal{L}^d(\mathbf{w},v)+\mathcal{D}(v,\mathbf{w})=0. \tag{3.15}
$$

Now we state the main theorem.

Theorem 3.1 *Let $c_f\in L^\infty(0,T;H^{k+3})$, $p\in L^\infty(0,T;H^{k+3})$, $\boldsymbol{s}\in L^\infty(0,T;(H^{k+2})^2)$, $\boldsymbol{u}\in L^\infty(0,T;(H^{k+2})^2)$, $\phi\in L^\infty(0,T;H^{k+3})$ be the exact solutions of the problem (3.1)–(3.6), and let c_h, p_h, $\mathbf{s}_h$, $\mathbf{u}_h$, ϕ_h be the numerical solutions of the semi-discrete LDG scheme*

(3.7)–(3.12) *with initial discretization given as* (3.13). *If the finite element space is the piecewise tensor product polynomials of degree at most k and h is sufficiently small, then we have the error estimate*

$$\begin{aligned}&\|c_f - c_h\|_{L^\infty(0,T;L^2)} + \|\mathbf{u} - \mathbf{u}_h\|_{L^\infty(0,T;L^2)} + \|\mathbf{s} - \mathbf{s}_h\|_{L^2(0,T;L^2)}\\ &+\|p - p_h\|_{L^\infty(0,T;L^2)} + \|\phi - \phi_h\|_{L^\infty(0,T;L^2)} \le Ch^{k+1},\end{aligned} \tag{3.16}$$

where the constant C is independent of h.

4 The Proof of the Main Theorem

In this section, we demonstrate the proof of Theorem 3.1. We first present some auxiliary results of the projections. Subsequently, we make an a priori error estimate which provides the boundedness of the numerical approximations. Then we construct the error equations which further yield several main energy inequalities and prove (3.16). Finally, the a priori error estimate are verified at the end of this section.

4.1 Projections and Interpolation Properties

In this section, we will present several useful lemmas of the projections. Let us start with the classical inverse properties [7].

Lemma 4.1 *Assume $u \in W_h^k$, then there exists a positive constant C independent of h and u such that*

$$h\|u\|_{\infty,K} + h^{1/2}\|u\|_{\Gamma_K} \le C\|u\|_K.$$

Lemma 4.2 *Suppose $w \in H^{k+1}(\Omega)$, then for any projection P_h, which is either P^+, Π_x^-, Π_y^- or P_k, we have*

$$\|w - P_h w\| + h^{1/2}\|w - P_h w\|_{\Gamma_h} \le Ch^{k+1}.$$

Moreover, the projection P^+ on the Cartesian meshes has the following superconvergence property [5].

Lemma 4.3 *Suppose $w \in H^{k+2}(\Omega)$, then for any $\boldsymbol{\rho} \in \mathbf{W}_h$ we have*

$$|\mathcal{D}(w - P^+ w, \boldsymbol{\rho})| \le Ch^{k+1}\|w\|_{k+2}\|\boldsymbol{\rho}\|. \tag{4.1}$$

In this paper, we use e to denote the error between the exact and numerical solutions, i.e. $e_c = c_f - c_h$, $e_p = p - p_h$, $\mathbf{e}_u = \mathbf{u} - \mathbf{u}_h$, $\mathbf{e}_s = \mathbf{s} - \mathbf{s}_h$, $\mathbf{e}_z = \mathbf{z} - \mathbf{z}_h$, $e_\phi = \phi - \phi_h$. As the general treatment of the finite element methods, we split the errors into two terms as

$$\begin{array}{lll} e_c = \xi_c - \eta_c, & \eta_c = P^+ c_f - c_f, & \xi_c = P^+ c_f - c_h,\\ e_p = \xi_p - \eta_p, & \eta_p = P^+ p - p, & \xi_p = P^+ p - p_h,\\ \mathbf{e}_u = \boldsymbol{\xi}_u - \boldsymbol{\eta}_u, & \boldsymbol{\eta}_u = \boldsymbol{\Pi}^- \mathbf{u} - \mathbf{u}, & \boldsymbol{\xi}_u = \boldsymbol{\Pi}^- \mathbf{u} - \mathbf{u}_h,\\ \mathbf{e}_s = \boldsymbol{\xi}_s - \boldsymbol{\eta}_s, & \boldsymbol{\eta}_s = \mathbf{P}_k \mathbf{s} - \mathbf{s}, & \boldsymbol{\xi}_s = \mathbf{P}_k \mathbf{s} - \mathbf{s}_h,\\ \mathbf{e}_z = \boldsymbol{\xi}_z - \boldsymbol{\eta}_z, & \boldsymbol{\eta}_z = \boldsymbol{\Pi}^- \mathbf{z} - \mathbf{z}, & \boldsymbol{\xi}_z = \boldsymbol{\Pi}^- \mathbf{z} - \mathbf{z}_h,\\ e_\phi = \xi_\phi - \eta_\phi, & \eta_\phi = P_k \phi - \phi, & \xi_\phi = P_k \phi - \phi_h. \end{array}$$

Based on the above notations, it is easy to verify that

$$\mathcal{L}^d(\boldsymbol{\eta}_u, v) = \mathcal{L}^d(\boldsymbol{\eta}_z, v) = 0, \quad \forall v \in Q^k(K). \tag{4.2}$$

Following [46–48,56] with some minor changes, we have the following lemma

Lemma 4.4 *Suppose ξ_c and $\boldsymbol{\xi}_s$ are defined above, we have*

$$\|\nabla \xi_c\| \le C(\|\boldsymbol{\xi}_s\| + h^{k+1}), \quad h^{-\frac{1}{2}}\|[\xi_c]\|_{\Gamma_h} \le C(\|\boldsymbol{\xi}_s\| + h^{k+1}).$$

Let us finish this section by proving the following lemma whose proof was given in [25].

Lemma 4.5 *Let $u \in C^{k+1}(\Omega)$ and $\Pi u \in W_h^k$. Suppose $\|u - \Pi u\| \le Ch^l$ for some positive constant C and $l \le k+1$. Then*

$$h\|u - \Pi u\|_\infty + h^{1/2}\|u - \Pi u\|_{\Gamma_h} \le Ch^l,$$

where the positive constant C does not depend on h.

4.2 A Priori Error Estimate

In this subsection, we would like to make an a priori error estimate assumption that

$$\|c_f - c_h\| + \|\phi - \phi_h\| + \|\phi_t - \phi_{ht}\| + \|\mathbf{u} - \mathbf{u}_h\| \le h^{\frac{3}{2}}, \tag{4.3}$$

which further implies

$$\|c_f - c_h\|_\infty + \|\phi - \phi_h\|_\infty + \|\phi_t - \phi_{ht}\|_\infty + \|\mathbf{u} - \mathbf{u}_h\|_\infty \le h^{\frac{1}{2}} \tag{4.4}$$

and

$$\|c_h\|_\infty + \|\phi_h\|_\infty + \|\phi_{ht}\|_\infty + \|\mathbf{u}_h\|_\infty \le C \tag{4.5}$$

by hypothesis 4 and Lemma 4.5. Moreover, by Hypothesis 1 and Lemma 2.1, we obtain

$$0 < C_* \le \phi_h \le C^*, \quad 0 < C_* \le \kappa^{-1}(\phi_h) \le C^*, \quad F(\phi_h) \le C, \quad max_{i,j}|D_{ij}| \le C. \tag{4.6}$$

Remark 4.1 The a priori estimate assumption (4.3) holds for small enough h and this choice is heavily based on how large the constant C is in (3.16). Notice that the constant C is independent of h, as long as h is sufficiently small, say $h < H$. Then we can guarantee (4.3) holds for $0 \le t \le T$. Moreover, we will show that, if $h < H$, then the equality of (4.3) cannot happen if $t < T$. However, we still need this estimate to obtain the boundedness of the numerical approximations. This assumption, which will be verified in Sect. 4.8, is used for the estimate of the convection terms.

4.3 Error Equations

In this subsection, we proceed to construct the error equations. From (3.7)–(3.12), we have the following error equations

$$\left(\gamma \frac{\partial e_p}{\partial t} + \frac{\partial e_\phi}{\partial t}, \zeta\right) = \mathcal{L}^d(\mathbf{e}_u, \zeta), \tag{4.7}$$

$$\left(\frac{\mu}{\kappa(\phi)}\mathbf{u} - \frac{\mu}{\kappa(\phi_h)}\mathbf{u}_h, \boldsymbol{\theta}\right) + \left(\frac{\rho}{\phi}\frac{\partial \mathbf{u}}{\partial t} - \frac{\rho}{\phi_h}\frac{\partial \mathbf{u}_h}{\partial t}, \boldsymbol{\theta}\right) + \left(\frac{\rho F(\phi)}{\sqrt{\kappa(\phi)}}|\mathbf{u}|\,\mathbf{u} - \frac{\rho F(\phi_h)}{\sqrt{\kappa(\phi_h)}}|\mathbf{u}_h|\,\mathbf{u}_h, \boldsymbol{\theta}\right) = \mathcal{D}(e_p, \boldsymbol{\theta}), \tag{4.8}$$

$$((\phi c_f)_t - (\phi_h c_h)_t, v) = \mathcal{L}^c(\mathbf{u}, c_f, v) - \mathcal{L}^c(\mathbf{u}_h, c_h, v) + \mathcal{L}^d(\mathbf{e}_z, v) - \big(A(a_v(\phi)c_f - a_v(\phi_h)c_h), v\big) + (f_p e_c, v), \tag{4.9}$$

$$(\mathbf{e}_s, \mathbf{w}) = \mathcal{D}(e_c, \mathbf{w}), \tag{4.10}$$

$$(\mathbf{e}_z, \boldsymbol{\psi}) = ((\mathbf{D}(\mathbf{u})\phi\mathbf{s} - \mathbf{D}(\mathbf{u}_h)\phi_h\mathbf{s}_h), \boldsymbol{\psi}), \tag{4.11}$$

$$(e_{\phi_t}, \beta) = (B(a_v(\phi)c_f - a_v(\phi_h)c_h), \beta), \tag{4.12}$$

for any $\zeta, v,\ \beta \in W_h^k$ and $\boldsymbol{\theta}, \mathbf{w},\ \boldsymbol{\psi} \in \mathbf{W}_h^k$.

In the following, we choose the same test functions as in [17], and obtain the energy inequalities. If the details are the same we skip them.

4.4 The First Energy Inequality

We take $v = \xi_c,\ \boldsymbol{w} = \boldsymbol{\xi}_z,\ \boldsymbol{\psi} = -\boldsymbol{\xi}_s$ in (4.9)–(4.11), respectively, and use Lemma 3.2 and (4.2), we can obtain

$$\tfrac{1}{2}\tfrac{d}{dt}\left(\phi_h\xi_c^2\right) + (\mathbf{D}(\mathbf{u}_h)\phi_h\xi_s, \xi_s) = R_1 + R_2 + R_3 + R_4 + R_5 + R_6, \tag{4.13}$$

where

$$\begin{aligned}
R_1 &= \left(\phi_h\frac{\partial\eta_c}{\partial t}, \xi_c\right) - (c_{f\,t}\xi_\phi, \xi_c) + (c_{f\,t}\eta_\phi, \xi_c) - (\phi_t\xi_c, \xi_c) + (\phi_t\eta_c, \xi_c)\\
&\quad -(c_h\xi_{\phi_t}, \xi_c) + (c_h\eta_{\phi_t}, \xi_c) + \frac{1}{2}((\phi_h)_t\xi_c, \xi_c)\\
R_2 &= -(\mathbf{D}(\mathbf{u})\mathbf{s}\xi_\phi, \boldsymbol{\xi}_s) + (\mathbf{D}(\mathbf{u})\mathbf{s}\eta_\phi, \boldsymbol{\xi}_s) + (\mathbf{D}(\mathbf{u})\phi_h\boldsymbol{\eta}_s, \boldsymbol{\xi}_s),\\
R_3 &= (\mathbf{u}c_f - \mathbf{u}_h c_h, \nabla\xi_c) + \sum_{e\in\Gamma_e}\langle \mathbf{u}c_f - \widehat{\mathbf{u}_h c_h}\cdot\boldsymbol{\nu}_e, [\xi_c]\rangle_e\\
R_4 &= -\mathcal{D}(\eta_c, \boldsymbol{\xi}_z),\\
R_5 &= (\boldsymbol{\eta}_s, \boldsymbol{\xi}_z) - (\boldsymbol{\eta}_z, \boldsymbol{\xi}_s) + (f_p e_c, \xi_c),\\
R_6 &= -(A(a_v(\phi)c_f - a_v(\phi_h)c_h), \xi_c),
\end{aligned}$$

where $\Gamma_e = \Gamma_0 \cup \partial\Omega_-$ and $\langle u, v\rangle_e = \int_e uv\, ds$. Now, we estimate each $R_i\ (i = 1, \ldots, 6)$ term. Using hypotheses 4 and (4.5), we can get

$$\begin{aligned}
R_1 &\le C\|\xi_c\|\left(\|\eta_{ct}\| + \|\xi_\phi\| + \|\eta_\phi\| + \|\xi_c\| + \|\eta_c\| + \|\xi_{\phi_t}\| + \|\eta_{\phi_t}\|\right)\\
&\le C\left(\|\xi_c\|^2 + \|\xi_\phi\|^2 + \|\xi_{\phi_t}\|^2 + h^{2k+2}\right),
\end{aligned} \tag{4.14}$$

where the second step requires Lemma 4.2. For R_2, by hypotheses h2, h4 and Lemma 4.2 and (4.6)

$$\begin{aligned}
R_2 &= -\left(\mathbf{D}(\mathbf{u})\mathbf{s}\xi_\phi, \boldsymbol{\xi}_s\right) + \left(\mathbf{D}(\mathbf{u})\mathbf{s}\eta_\phi, \boldsymbol{\xi}_s\right) - (\mathbf{D}(\mathbf{u}_h)\phi_h\boldsymbol{\eta}_s, \boldsymbol{\xi}_s) + ((\mathbf{D}(\mathbf{u}) - \mathbf{D}(\mathbf{u}_h))\phi_h\boldsymbol{\eta}_s, \boldsymbol{\xi}_s)\\
&\le C\|\boldsymbol{\xi}_s\|\left(\|\xi_\phi\| + \|\eta_\phi\| + \|\boldsymbol{\eta}_s\|\right) + C\|\mathbf{u} - \mathbf{u}_h\|\|\boldsymbol{\xi}_s\|\\
&\le C\left(\|\xi_\phi\|^2 + \|\boldsymbol{\xi}_u\|^2 + h^{2k+2}\right) + \epsilon\|\boldsymbol{\xi}_s\|^2.
\end{aligned} \tag{4.15}$$

The estimate of R_3 is the same with [17], here we present the result.

$$\begin{aligned}
R_3 &\le C\left(h^{k+1} + \|\boldsymbol{\xi}_u\| + \|\xi_c\|\right)\left(\|\boldsymbol{\xi}_s\| + h^{k+1}\right)\\
&\le C\left(\|\boldsymbol{\xi}_u\|^2 + \|\xi_c\|^2 + h^{2k+2}\right) + \epsilon\|\boldsymbol{\xi}_s\|^2.
\end{aligned} \tag{4.16}$$

We estimate R_4 by Lemmas 4.3 and 4.2

$$R_4 \le Ch^{k+1}\|c_f\|_{k+2}\|\boldsymbol{\xi}_z\| \le Ch^{2k+2} + \epsilon\|\boldsymbol{\xi}_z\|^2. \tag{4.17}$$

Use Hypotheses 4 and Lemma 4.2 to obtain

$$\begin{aligned} R_5 &\le \|\boldsymbol{\eta}_s\|\|\boldsymbol{\xi}_z\| + \|\boldsymbol{\eta}_z\|\|\boldsymbol{\xi}_s\| + C\|e_c\|\|\xi_c\| \\ &\le C\left(\|\xi_c\|^2 + h^{2k+2}\right) + \epsilon\left(\|\boldsymbol{\xi}_s\|^2 + \|\boldsymbol{\xi}_z\|^2\right). \end{aligned} \tag{4.18}$$

Finally, we estimate R_6,

$$\begin{aligned} R_6 &= -\left(A(a_v(\phi)(c_f - c_h), \xi_c\right) - (Ac_h(a_v(\phi) - a_v(\phi_h), \xi_c)) \\ &\le C\|\xi_c\|\|c_f - c_h\| + C\|\xi_c\|\|\phi - \phi_h\| \\ &\le C\left(\|\xi_c\|^2 + \|\xi_\phi\|^2 + h^{2k+2}\right), \end{aligned} \tag{4.19}$$

where the second step follows from hypothesis 4, Lemma 2.1 and (4.5), and the last step requires Lemma 4.2.

Substituting the estimation (4.14)–(4.19) into (4.13) and use hypothesis 2 and (4.6), we obtain

$$\begin{aligned} \frac{d\|\sqrt{\phi_h}\xi_c\|^2}{\partial t} + \|\boldsymbol{\xi}_s\|^2 \le C&\left(\|\xi_c\|^2 + \|\xi_\phi\|^2 + \|\xi_{\phi_t}\|^2 + \|\boldsymbol{\xi}_u\|^2 + h^{2k+2}\right) \\ &+ \epsilon\left(\|\boldsymbol{\xi}_s\|^2 + \|\boldsymbol{\xi}_z\|^2\right). \end{aligned} \tag{4.20}$$

Now we proceed to eliminate $\|\xi_z\|$ on the right-hand side of the above equation. Take $\boldsymbol{\psi} = \boldsymbol{\xi}_z$ in (4.11) to obtain

$$\begin{aligned} (\boldsymbol{\xi}_z, \boldsymbol{\xi}_z) &= (\boldsymbol{\eta}_z, \boldsymbol{\xi}_z) + (\mathbf{D}(\mathbf{u})\mathbf{s}\phi - \mathbf{D}(\mathbf{u}_h)\mathbf{s}_h\phi_h), \boldsymbol{\xi}_z), \\ &= (\boldsymbol{\eta}_z, \boldsymbol{\xi}_z) + (\mathbf{D}(\mathbf{u})\mathbf{s}(\phi - \phi_h), \boldsymbol{\xi}_z) + ((\mathbf{D}(\mathbf{u}) \\ &\quad - \mathbf{D}(\mathbf{u}_h))\phi_h\mathbf{s}, \boldsymbol{\xi}_z) + (\mathbf{D}(\mathbf{u}_h)\phi_h(\mathbf{s} - \mathbf{s}_h), \boldsymbol{\xi}_z), \end{aligned}$$

which further implies

$$\begin{aligned} \|\boldsymbol{\xi}_z\|^2 &\le \|\boldsymbol{\eta}_z\|\|\boldsymbol{\xi}_z\| + C\|\phi - \phi_h\|\|\boldsymbol{\xi}_z\| + C\|\mathbf{u} - \mathbf{u}_h\|\|\boldsymbol{\xi}_z\| + C\|\mathbf{s} - \mathbf{s}_h\|\|\boldsymbol{\xi}_z\| \\ &\le C\left(\|\xi_\phi\|^2 + \|\boldsymbol{\xi}_u\|^2 + \|\boldsymbol{\xi}_s\|^2 + h^{2k+2}\right) + \epsilon\|\boldsymbol{\xi}_z\|^2, \end{aligned}$$

where in the first step we applied hypotheses 3, 4 and (4.6), the second step follows from Lemma 4.2. Take ϵ to be small, we have

$$\|\boldsymbol{\xi}_z\|^2 \le C\left(\|\xi_\phi\|^2 + \|\boldsymbol{\xi}_u\|^2 + \|\boldsymbol{\xi}_s\|^2 + h^{2k+2}\right).$$

Substituting the above equation into (4.20), then integrating with respect to t and use (4.6), we have the first energy inequality

$$\|\xi_c\|^2 + \int_0^t \|\boldsymbol{\xi}_s\|^2\, dt \le C\int_0^t \left(\|\xi_c\|^2 + \|\xi_\phi\|^2 + \|\xi_{\phi_t}\|^2 + \|\boldsymbol{\xi}_u\|^2\right) dt + Ch^{2k+2}. \tag{4.21}$$

Now we derive the energy inequality for p and $\mathbf{u}$ by studying equations (4.7), (4.8).

4.5 The Second Energy Inequality

In this subsection, we will derive the second energy inequality. Taking $\zeta = \xi_p, \boldsymbol{\theta} = \boldsymbol{\xi}_u$ in (4.7) and (4.8), respectively, and using Lemma 3.2 and (4.2), we can obtain

$$\begin{aligned}&\left(\gamma\frac{\partial\xi_p}{\partial t},\xi_p\right)+\frac{1}{2}\frac{d}{dt}\left(\frac{\rho}{\phi_h}\boldsymbol{\xi}_u^2\right)+\left(\frac{\mu}{\kappa(\phi_h)}\boldsymbol{\xi}_u,\boldsymbol{\xi}_u\right)+\left(\frac{\rho F(\phi)}{\kappa(\phi)}(|\mathbf{u}|\mathbf{u}-|\mathbf{u}_h|\mathbf{u}_h),\mathbf{e}_u\right)\\&=T_1+T_2-T_3-T_4-T_5-T_6,\end{aligned}\tag{4.22}$$

where

$$\begin{aligned}T_1&=\left(\gamma\frac{\partial\eta_p}{\partial t},\xi_p\right)-(\xi_{\phi_t},\xi_p)+(\eta_{\phi_t},\xi_p)\\T_2&=-\left(\mu\left(\frac{1}{\kappa(\phi)}-\frac{1}{\kappa(\phi_h)}\right)\mathbf{u},\boldsymbol{\xi}_u\right)+\left(\frac{\mu}{\kappa(\phi_h)}\boldsymbol{\eta}_u,\boldsymbol{\xi}_u\right),\\T_3&=\left(\rho\mathbf{u}_t\left(\frac{1}{\phi}-\frac{1}{\phi_h}\right),\boldsymbol{\xi}_u\right)-\left(\frac{\rho}{\phi_h}\frac{\partial\boldsymbol{\eta}_u}{\partial t},\boldsymbol{\xi}_u\right)-\frac{1}{2}\left(\frac{d}{dt}\left(\frac{1}{\phi_h}\right)\rho\boldsymbol{\xi}_u,\boldsymbol{\xi}_u\right)\\T_4&=\left(\frac{\rho F(\phi)}{\sqrt{K(\phi)}}(|\mathbf{u}|\mathbf{u}-|\mathbf{u}_h|\mathbf{u}_h),\boldsymbol{\eta}_u\right),\\T_5&=\left(\left(\frac{\rho F(\phi)}{\sqrt{\kappa(\phi)}}-\frac{\rho F(\phi_h)}{\sqrt{\kappa(\phi_h)}}\right)|\mathbf{u}_h|\mathbf{u}_h,\boldsymbol{\xi}_u\right),\\T_6&=\mathcal{D}(\eta_p,\boldsymbol{\xi}_u)\end{aligned}$$

Now, we estimate T_i $(i=1,\ldots,6)$ term by term. Using Lemma 4.2, we can get

$$T_1\le C\|\xi_p\|\left(\|\eta_{p_t}\|+\|\xi_{\phi_t}\|+\|\eta_{\phi_t}\|\right)\le C\left(\|\xi_p\|^2+\|\xi_{\phi_t}\|^2+h^{2k+2}\right),\tag{4.23}$$

Use Lemmas 2.1, 4.2, (4.6) and hypotheses 4 to obtain

$$T_2\le C\|\boldsymbol{\xi}_u\|\|\boldsymbol{\eta}_u\|+C\|\boldsymbol{\xi}_u\|\|\phi-\phi_h\|\le C\left(\|\xi_u\|^2+\|\xi_\phi\|^2+h^{2k+2}\right).\tag{4.24}$$

Using hypothesis 4, (4.5) and (4.6) we estimate T_3 by

$$T_3\le C\|\boldsymbol{\xi}_u\|\|\phi-\phi_h\|+C\|\boldsymbol{\xi}_u\|\|\boldsymbol{\eta}_{u_t}\|+C\|\boldsymbol{\xi}_u\|^2\le C\|\boldsymbol{\xi}_u\|^2+\|\xi_\phi\|^2+h^{2k+2},\tag{4.25}$$

where the second step requires Lemma 4.2.

The estimate of T_4, T_5 also requires hypothesis 4, (4.5) and Lemma 4.2

$$\begin{aligned}T_4&=\left(\frac{\rho F(\phi)}{\sqrt{\kappa(\phi)}}|\mathbf{u}|(\mathbf{u}-\mathbf{u}_h),\boldsymbol{\eta}_u\right)+\left(\frac{\rho F(\phi)}{\sqrt{\kappa(\phi)}}\mathbf{u}_h(|\mathbf{u}|-|\mathbf{u}_h|),\boldsymbol{\eta}_u\right)\\&\le C\|\boldsymbol{u}-\boldsymbol{u}_h\|\|\boldsymbol{\eta}_u\|\\&\le C\left(\|\boldsymbol{\xi}_u\|+\|\boldsymbol{\eta}_u\|\right)\|\boldsymbol{\eta}_u\|\le C\left(\|\boldsymbol{\xi}_u\|^2+h^{2k+2}\right).\end{aligned}\tag{4.26}$$

$$\begin{aligned}T_5&=\left(\rho|\mathbf{u}_h|\mathbf{u}_h\left(\frac{F(\phi)}{\sqrt{\kappa(\phi)}}-\frac{F(\phi_h)}{\sqrt{\kappa(\phi_h)}}\right),\boldsymbol{\xi}_u\right)\\&=\left(\rho|\mathbf{u}_h|\mathbf{u}_h\left(\frac{F(\phi)}{\sqrt{\kappa(\phi)}}-\frac{F(\phi_h)}{\sqrt{\kappa(\phi)}}+\frac{F(\phi_h)}{\sqrt{\kappa(\phi)}}-\frac{F(\phi_h)}{\sqrt{\kappa(\phi_h)}}\right),\boldsymbol{\xi}_u\right)\end{aligned}$$

$$= \left(\rho|\mathbf{u}_h|\mathbf{u}_h \frac{F(\phi)-F(\phi_h)}{\sqrt{\kappa(\phi)}}, \boldsymbol{\xi}_u\right) + \left(\rho|\mathbf{u}_h|\mathbf{u}_h F(\phi_h)\left(\frac{1}{\sqrt{\kappa(\phi)}} - \frac{1}{\sqrt{\kappa(\phi_h)}}\right), \boldsymbol{\xi}_u\right)$$
$$\leq C\|\phi-\phi_h\|\|\boldsymbol{\xi}_u\| \leq C\left(\|\xi_\phi\|^2 + \|\boldsymbol{\xi}_u\|^2 + h^{2k+2}\right). \tag{4.27}$$

Finally, we estimate T_6,

$$T_6 = \mathcal{D}(\eta_p, \boldsymbol{\xi}_u) \leq Ch^{2k+2}\|\eta_p\|_{k+2}\|\boldsymbol{\xi}_u\| \leq C\left(\|\boldsymbol{\xi}_u\|^2 + h^{2k+2}\right), \tag{4.28}$$

where the first step follows from Lemma 4.3.

Substituting (4.23)–(4.28) into (4.22), we have

$$\left\|\frac{\mu^{1/2}}{\kappa^{\frac{1}{2}}(\phi_h)}\boldsymbol{\xi}_u\right\|^2 + \frac{1}{2}\frac{d}{dt}\|\gamma^{1/2}\xi_p\|^2 + \frac{1}{2}\frac{d}{dt}\left\|\frac{\rho^{1/2}}{\phi_h^{1/2}}\boldsymbol{\xi}_u\right\|^2 + \left(\frac{\rho F(\phi)}{\sqrt{\kappa(\phi)}}(|\mathbf{u}|\,\mathbf{u} - |\mathbf{u}_h|\,\mathbf{u}_h), e_u\right)$$
$$\leq C\left(\|\xi_p\|^2 + \|\xi_{\phi_t}\|^2 + \|\xi_\phi\|^2 + \|\boldsymbol{\xi}_u\|^2 + h^{2k+2}\right).$$

Thanks to [31] Lemma 3.2, $\left(\frac{\rho F(\phi)}{\sqrt{\kappa(\phi)}}(|\mathbf{u}|\,\mathbf{u} - |\mathbf{u}_h|\,\mathbf{u}_h), e_{\mathbf{u}}\right) \geq 0$, the above equation results in

$$\frac{d}{dt}\|\gamma^{1/2}\xi_p\|^2 + \frac{d}{dt}\left\|\frac{\rho^{1/2}}{\phi_h^{1/2}}\boldsymbol{\xi}_u\right\|^2$$
$$\leq C\left(\|\xi_p\|^2 + \|\xi_{\phi_t}\|^2 + \|\xi_\phi\|^2 + \|\boldsymbol{\xi}_u\|^2 + h^{2k+2}\right).$$

Integrating the above equation with respect to t and using (4.6), we obtain

$$\|\xi_p\|^2 + \|\boldsymbol{\xi}_u\|^2 \leq C\int_0^t \left(\|\xi_p\|^2 + \|\xi_{\phi_t}\|^2 + \|\xi_\phi\|^2 + \|\boldsymbol{\xi}_u\|^2\right) dt + Ch^{2k+2}. \tag{4.29}$$

4.6 The Third Energy Inequality

The third energy inequality will be derived by taking $\beta = \xi_\phi$ in (4.12)

$$(\xi_{\phi_t}, \xi_\phi) = (\eta_{\phi_t}, \xi_\phi) + \left(Ba_v(\phi)c_f - Ba_v(\phi_h)c_h, \xi_\phi\right)$$
$$= (\eta_{\phi_t}, \xi_\phi) + \left(Ba_v(\phi)(c_f - c_h), \xi_\phi\right) + \left(Bc_h(a_v(\phi) - a_v(\phi_h)), \xi_\phi\right),$$

which further yields

$$\frac{1}{2}\frac{d}{dt}\|\xi_\phi\|^2 \leq \|\eta_{\phi_t}\|\|\xi_\phi\| + C\|c_f - c_h\|\|\xi_\phi\| + C\|\phi-\phi_h\|\|\xi_\phi\|$$
$$\leq C\left(\|\xi_\phi\|^2 + \|\xi_c\|^2 + h^{2k+2}\right),$$

where we have used Lemma 2.1 and (4.5). Integrating the above inequality with respect to t, we obtain the third energy inequality

$$\|\xi_\phi\|^2 \leq C\int_0^t \left(\|\xi_\phi\|^2 + \|\xi_c\|^2\right) dt + Ch^{2k+2}. \tag{4.30}$$

4.7 The Fourth Energy Inequality

We take $\beta = \xi_{\phi_t}$ in (4.12) to obtain the last energy inequality

$$\begin{aligned}(\xi_{\phi_t}, \xi_{\phi_t}) &= (\eta_{\phi_t}, \xi_{\phi_t}) + \left(Ba_v(\phi)c_f - Ba_v(\phi_h)c_h, \xi_{\phi_t}\right) \\ &= (\eta_{\phi_t}, \xi_{\phi_t}) + \left(Ba_v(\phi)(c_f - c_h), \xi_{\phi_t}\right) + \left(Bc_h(a_v(\phi) - a_v(\phi_h)), \xi_{\phi_t}\right).\end{aligned}$$

Then we have

$$\begin{aligned}\|\xi_{\phi_t}\|^2 &\le \|\eta_{\phi_t}\|\|\xi_{\phi_t}\| + C\|c_f - c_h\|\|\xi_{\phi_t}\| + C\|\phi - \phi_h\|\|\xi_{\phi_t}\| \\ &\le C\left(\|\xi_c\|^2 + \|\xi_\phi\|^2 + h^{2k+2}\right) + \epsilon\|\xi_{\phi_t}\|^2,\end{aligned}$$

which further yields the last energy inequality

$$\|\xi_{\phi_t}\|^2 \le C\left(\|\xi_c\|^2 + \|\xi_\phi\|^2 + h^{2k+2}\right). \tag{4.31}$$

4.8 Proof of Theorem 3.1

Now we are ready to combine the four energy inequalities and finish the proof of Theorem 3.1.

Firstly, from (4.21), (4.29) and (4.30), it is easy to derive the following estimate

$$\begin{aligned}&\|\xi_c\|^2 + \|\xi_p\|^2 + \left\|\boldsymbol{\xi}_u\right\|^2 + \|\xi_\phi\|^2 + \int_0^t \|\boldsymbol{\xi}_s\|^2\, dt \\ &\le C\int_0^t \left(\|\xi_c\|^2 + \|\xi_p\|^2 + \left\|\boldsymbol{\xi}_u\right\|^2 + \|\xi_\phi\|^2 + \|\xi_{\phi_t}\|^2\right) dt + Ch^{2k+2}.\end{aligned}$$

Thanks to (4.31), we can eliminate ξ_{ϕ_t} in the above inequality to obtain

$$\begin{aligned}&\|\xi_c\|^2 + \|\xi_p\|^2 + \left\|\boldsymbol{\xi}_u\right\|^2 + \|\xi_\phi\|^2 + \int_0^t \|\boldsymbol{\xi}_s\|^2\, dt \\ &\le C\int_0^t \left(\|\xi_c\|^2 + \|\xi_p\|^2 + \left\|\boldsymbol{\xi}_u\right\|^2 + \|\xi_\phi\|^2\right) dt + Ch^{2k+2}.\end{aligned}$$

Now, we can employ Gronwall's inequality to obtain

$$\|\xi_c\|^2 + \|\xi_p\|^2 + \|\boldsymbol{\xi}_u\|^2 + \|\xi_\phi\|^2 + \int_0^t \|\boldsymbol{\xi}_s\|^2\, dt \le Ch^{2k+2}. \tag{4.32}$$

For the boundness of ϕ_{h_t},

$$\|\xi_{\phi_t}\| \le C\left(\|\xi_c\| + \|\xi_\phi\| + h^{k+1}\right) \le Ch^{k+1}. \tag{4.33}$$

Combining (4.33) and Lemma 4.2, we have

$$\|\phi_t - \phi_{h_t}\| \le \|\xi_{\phi_t}\| + \|\eta_{\phi_t}\| \le Ch^{k+1}.$$

Finally, by using the standard approximation result, we obtain (3.16). To complete the proof, let us verify the a priori assumption (4.3). For $k \ge 1$, we can consider h small enough so that $Ch^{k+1} < \frac{1}{2}h^{\frac{3}{2}}$, where C is the constant determined by the final time T. Then define $t^* = \inf\{t : \|c_f - c_h\| + \|\phi - \phi_h\| + \|\phi_t - \phi_{h_t}\| + \|\boldsymbol{u} - \boldsymbol{u}_h\| \ge h^{\frac{3}{2}}\}$, we should have $\|c_f - c_h\| + \|\phi - \phi_h\| + \|\phi_t - \phi_{h_t}\| + \|\boldsymbol{u} - \boldsymbol{u}_h\| = h^{\frac{3}{2}}$ by continuity in time at $t = t^*$. However, if $t^* < T$, theorem 3.1 implies that $\|c - c_h\| + \|\phi - \phi_h\| + \|\phi_t - \phi_{h_t}\| + \|\boldsymbol{u} - \boldsymbol{u}_h\| \le Ch^{k+1}$

for $t \leq t^*$, in particular $h^{\frac{3}{2}} = \|(c - c_h)(t^*)\| + \|(\phi - \phi_h)(t^*)\| + \|(\phi_t - \phi_{h_t})(t^*)\| + \|(\boldsymbol{u} - \boldsymbol{u}_h)(t^*)\| \leq Ch^{k+1} < \frac{1}{2}h^{\frac{3}{2}}$, which is a contradiction. Therefore, there always holds $t^* \geq T$, and thus the a priori assumption (4.3) is justified.

Since the LDG spatial discretization allows a mesh with hanging nodes, we employ mesh adaptation to save computational cost. That is during the simulation, fine mesh is used for a region while coarse mesh for the rest of the computational domain. We discuss the mesh adaptation in the following section.

5 Mesh Adaptation

In this section mesh adaptation for the equations modelling wormhole propagations will be studied. We will first discuss refinement and coarsening of quadrilaterals, subsequently we provide a trouble indicator to select candidate elements in the computational mesh for refinement and coarsening. Finally mesh adaptation procedure will be presented.

5.1 Refinement and Coarsening of Quadrilaterals

In this section we will discuss the refinement of a single quadrilateral and coarsening of the children quadrilaterals which are refined from the same quadrilateral. As [42], we assume that

- the initial computational mesh is composed by uniform rectangular elements which are labeled as level with zero, namely $Level = 0$,
- each element in the computational mesh can be refined at most LEV times,
- an element, called parent element, when is refined in necessary is divided into four child elements with equal size, and

$$Level \text{ of the child elements} = Level \text{ of the parent element} + 1,$$

- the four child elements which all of them are to be coarsened, obtained from the same parent element, can be coarsened to the parent element,
- the difference of $Level$ of an element between its direct neighboring elements are at most 1.

The projections between parent element and its four child elements are defined in [42,61].

To start the mesh adaption, we require a trouble indicator for to refine a element or coarsening the child elements.

5.2 Trouble Indicator for Refinement and Coarsening

In this section, we will provide a trouble indicator to select candidate elements in the computational mesh for refinement and coarsening. Since the value of the physical variable changes rapidly in some area, then the elements in this region need to be refined. As the topology of the flow field changes, elements which were refined from the parent element, have no change anymore, need to be coarsened.

The trouble indicator η^K for each element K is defined based on the jump of the concentration c_{f_h} and porosity ϕ_h between K and its direct and indirect neighbor, given by

$$\eta^K = \max\left\{\frac{|\phi_h(K)-\phi_h(K_n)|}{\text{diam}(K)}, \frac{|c_{f_h}(K)-c_{f_h}(K_n)|}{\text{diam}(K)}\right\},$$
$$\text{for all } K_n \text{ with } K_n \text{ a neighbor of } K \text{ of degree at most } m. \tag{5.1}$$

Here $\phi_h(K), c_h(K)$ represent the porosity and concentration in the center of an element K, respectively. And $\text{diam}(K)$ means the longest edge of element K. The definition of neighbor of degree m of element K^j is defined in [13,42]. Use of indirect neighbor of an element is to guarantee the stability of the numerical scheme on the adaptive mesh.

Based on the trouble indicator for the elements in the computational mesh, we select candidate elements for refinement and coarsening. For each element K in the computational mesh,

$$\begin{aligned}&\text{if } \eta^K > \eta_{upp} \text{ and the level of } K < LEV\\ &\quad \text{then we mark } K \text{ as a candidate element for refinement,}\\ &\text{elseif } \eta^K < \eta_{low} \text{ and the level of } K > 0\\ &\quad \text{then we mark } K \text{ as a candidate element for coarsening,}\end{aligned} \tag{5.2}$$

with problem dependent parameters η_{upp}, η_{low} and $\eta_{upp} > \eta_{low} > 0$.

5.3 Strategy for Refinement and Coarsening

In this section we will present a refinement and coarsening strategy for the LDG discretization, given candidate elements selected through the trouble indicator (5.2). To guarantee the difference in the refinement levels between two neighboring elements less than two, "refinement must, coarsening can" strategy is used for the candidate elements. This strategy means that a candidate element K for refinement is definitely refined and refinement of its neighbor elements depends on the difference in their refinement levels. While coarsening of a candidate element K is more complex, it is related with the neighboring elements of K refined from the same parent element, and the level difference between K and all of its neighbor. If one of the child element of K's parent element is not a candidate coarsening element, then K should not be coarsened. If the level difference between K and one of its neighbor is one, K should not be coarsened either. We refer the readers [42] for more details of the strategy for mesh adaptation.

6 Numerical Example

In this section, we perform several numerical examples to illustrate the accuracy and capability of the LDG schemes for the modelling equations of wormhole propagations in Sect. 3.3. We study the numerical examples of real wormhole propagation scenario in petroleum engineering in Sect. 6.2. A similar wormhole propagation problem was studied in [17] where the modelling equations (2.1) with $\gamma = 0$ and a equation different from (2.2) for the velocity $\mathbf{u}$. In [17], an explicit time discretization was used with the time step as $\delta t = O(h^2)$, which is not practical for two-dimensional simulations, especially for fine resolution and long time simulations.

Suppose the coefficients of the polynomial expansions of numerical variables are collected in the vector $\widehat{\mathbf{U}}(t)$. The LDG discretization (3.7)–(3.12) results in an ODEs system

$$\frac{\partial \widehat{\mathbf{U}}}{\partial t} = \mathcal{F}(\widehat{\mathbf{U}}, t). \tag{6.1}$$

Subsequently various time schemes can be applied to solve it. For the accuracy test, the third order explicit strong-stability-preserving Runge–Kutta method [39] is used, given by

$$\begin{aligned}
\widehat{\mathbf{U}}^{(1)} &= \widehat{\mathbf{U}}^n + \Delta t \mathbf{L}(\widehat{\mathbf{U}}^n),\\
\widehat{\mathbf{U}}^{(2)} &= \frac{3}{4}\widehat{\mathbf{U}}^n + \frac{1}{4}\left(\widehat{\mathbf{U}}^{(1)} + \Delta t \mathbf{L}(\widehat{\mathbf{U}}^{(1)})\right),\\
\widehat{\mathbf{U}}^{n+1} &= \frac{1}{3}\widehat{\mathbf{U}}^n + \frac{2}{3}\left(\widehat{\mathbf{U}}^{(2)} + \Delta t \mathbf{L}(\widehat{\mathbf{U}}^{(2)})\right),
\end{aligned}$$

We take the time step to be sufficiently small as $\delta t = O(h^2)$ such that the error in time is negligible compared to spatial error. While for the real wormhole propagation problem, we apply a first-order semi-implicit time discretization to solve (6.1), given by:

$$\begin{aligned}
&\left(\gamma \frac{p^{n+1} - p^n}{\delta t_n}, \zeta\right)_K + \left(\frac{\phi^{n+1} - \phi^n}{\delta t_n}, \zeta\right)_K + (\nabla \cdot \mathbf{u}^{n+1}, \zeta)_K = (f(x, t_n), \zeta)_K,\\
&\left(\frac{\rho}{\phi^{n+1}} \frac{\mathbf{u}^{n+1} - \mathbf{u}^n}{\delta t_n}, \boldsymbol{\theta}\right)_K + \left(\frac{\mu}{\kappa(\phi^{n+1})}\mathbf{u}^{n+1}, \boldsymbol{\theta}\right)_K + \left(\frac{\rho F(\phi_h^{n+1})}{\sqrt{\kappa(\phi^{n+1})}} \left|\mathbf{u}^n\right| \mathbf{u}^{n+1}, \boldsymbol{\theta}\right)_K\\
&\quad = -(\nabla p^{n+1}, \boldsymbol{\theta})_K + (\rho \mathbf{g}, \boldsymbol{\theta})_K,\\
&\left(\frac{(\phi c_f)^{n+1} - (\phi c_f)^n}{\delta t_n}, v\right)_K + (\nabla \cdot (\mathbf{u}^n c_f^n + \mathbf{z}^{n+1}), v)_K\\
&\quad = -(A a_v(\phi^{n+1}) c_f^n, v)_K + (f_p c_f^n + f_I c_I, v)_K,\\
&(\mathbf{s}^{n+1}, \mathbf{w})_K = -(\nabla c_f^{n+1}, \mathbf{w})_K,\\
&(\mathbf{z}^{n+1}, \boldsymbol{\psi})_K = (\phi^{n+1} \mathbf{D}(\mathbf{u}^n) \mathbf{s}^{n+1}, \boldsymbol{\psi})_K,\\
&\left(\frac{\phi^{n+1} - \phi^n}{\delta t_n}, \beta\right)_K = (B a_v(\phi^n) \widetilde{c_f^n}, \beta)_K.
\end{aligned}$$

Here

$$\widetilde{c_f^n} = min\{1, max\{0, c_f\}\}.$$

Physically, c_f is the volumetric concentration of the acid and it should be between 0 and 1. To make the numerical solution to be physically relevant, we use the cut-off technique for c_f.

6.1 Accuracy Test

Example 6.1 We solve (2.1)–(2.4) and the parameters are taken as

$$\begin{aligned}
&d_m = 10^{-2}, \quad \alpha_l = 0.1, \quad \alpha_t = 0.1, \quad K_0 = 1, \quad T = 0.1,\\
&\alpha = k_c = k_s = \mu = f_I = 1, \quad \rho = 1, \quad g = 0,\\
&a_0 = 0.5, \quad \rho_s = 10, \quad \gamma = 1,
\end{aligned} \tag{6.2}$$

where $\mathbf{I}$ is the identity matrix.

The exact smooth solutions are given as

Table 1 Accuracy test for pressure and velocity in Example 6.1

	M	$\|\|p - p_h\|\|$	Order	$\|\|u - u_h\|\|$	Order	$\|\|c_f - c_{f_h}\|\|$	Order	$\|\|\phi - \phi_h\|\|$	Order
P^1	10	5.28E−1	–	8.42E−1	–	1.65E−1	–	2.41E−2	–
	20	1.91E−1	1.46	2.41E−1	1.80	3.63E−2	2.18	6.10E−3	1.98
	40	2.67E−2	2.83	7.75E−2	1.63	7.41E−3	2.29	1.53E−3	2.00
	80	5.77E−3	2.21	1.38E−2	2.48	1.68E−3	2.13	3.82E−4	2.00
P^2	10	1.94E−1	–	1.79E−1	–	3.64E−2	–	2.43E−3	–
	20	2.71E−2	2.84	3.25E−2	2.46	3.11E−3	3.55	3.08E−4	2.98
	40	2.97E−3	3.19	4.12E−3	2.98	3.07E−4	3.34	3.86E−5	2.99
	80	3.99E−4	2.89	5.08E−4	3.02	2.42E−5	3.66	4.82E−6	3.00

$$
\begin{aligned}
&p(\mathbf{x}, t) = e^{-t}\cos(x)\cos(y),\\
&u_1(\mathbf{x}, t) = 1.5 + e^{-t}\sin^2(x)\cos(2y), \quad u_2(\mathbf{x}, t) = 1.5 + e^{-t}\sin^2(x)\sin(2y)\\
&\phi(\mathbf{x}, t) = 0.6 + t\sin(x)\cos(y), \quad c_f(\mathbf{x}, t) = 0.5 + 0.4e^{-t}\sin(x)\sin(y). \qquad (6.3)
\end{aligned}
$$

We can calculate the initial conditions and the right hand sides accordingly. Piecewise linear and quadratic tensor product polynomials are employed in the LDG scheme. We perform accuracy verifications on uniform meshes with $M \times M$ elements over the computational domain $\Omega = [0, 2\pi] \times [0, 2\pi]$, and compute the numerical approximations at $T = 0.1$. Periodic boundary condition is used in this numerical example. The numerical results are given in Table 1. From the table, we can observe optimal convergence rates, which verifies the results in Theorem 3.1.

The next two examples are simulations of real wormhole propagation scenario in petroleum engineering.

6.2 Wormhole Propagation Problem

The computational domain is $\Omega = [0, 0.2\,\text{m}] \times [0, 0.2\,\text{m}]$. Initial concentration of acid and initial porosity of rock in this domain are set to be $c_0 = 0$ and $\phi_0 = 0.2$, respectively. The acid flow is injected to the porous media from the left boundary with a velocity of $u = 0.01\,\text{m/s}$ and drained out of it from the right boundary with the same velocity. Top and bottom boundary conditions are set to be periodic. The concentration of influx acid is $10\,\text{mol/m}^2$. To observe the wormhole propagation, we set two singular areas with high porosity and permeability on the left boundary with size to be $0.01\,\text{m} \times 0.01\,\text{m}$: one is 0.05 m above the bottom with the porosity of 0.4, and the other 0.1 m above the bottom with the porosity of 0.6. The permeability of the two entries is determined by (2.7) which is about $10^{-10}\,\text{m}^2$ and $10^{-11}\,\text{m}^2$, respectively. For the real wormhole propagation examples, the time step is chosen as $\delta t = 0.2\,h$ in the semi-implicit time discretization.

We use mesh adaptation discussed in Sect. 5 to save computational costs in the simulations. We choose $m = 2$ in (5.1) the defination of trouble indicator η^K and $\eta^{upp} = 5$, $\eta_{low} = 0.05$ in (5.2) for candidate elements for refinement and coarsening in the following two examples. We remark that the values of η^{upp}, η^{low} can vary little bit and give similar numerical results.

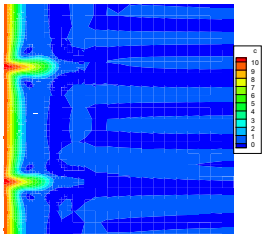

(a) c_{f_h} at $T = 20$

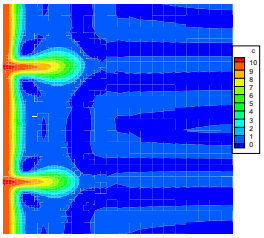

(b) c_{f_h} at $T = 35$

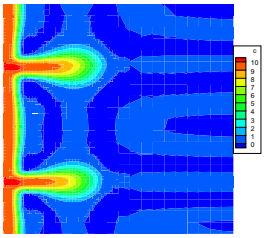

(c) c_{f_h} at $T = 50$

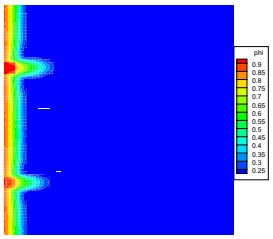

(d) ϕ_h at $T = 20$

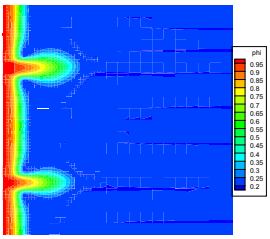

(e) ϕ_h at $T = 35$

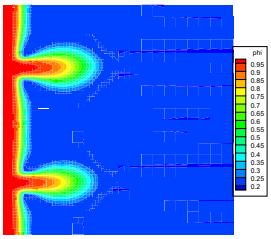

(f) ϕ_h at $T = 50$

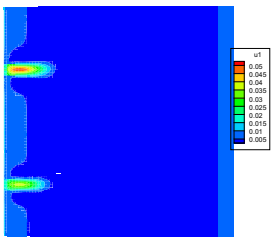

(g) u_{1h} at $T = 20$

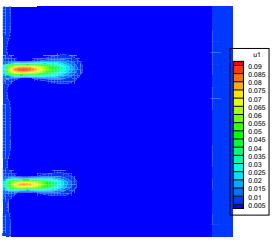

(h) u_{1h} at $T = 35$

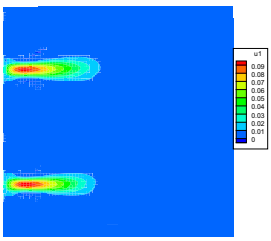

(i) u_{1h} at $T = 50$

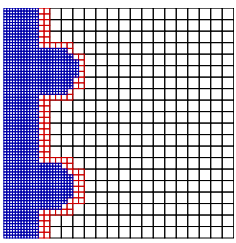

(j) $T = 20$, adaptive mesh

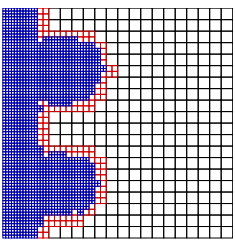

(k) $T = 35$, adaptive mesh

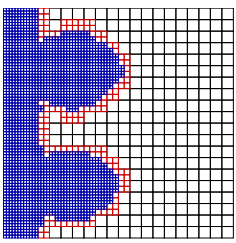

(l) $T = 50$, adaptive mesh

Fig. 1 Example 2: numerical solutions for concentration, porosity and velocity in x direction with time evolution, the initial adaptive mesh is composed by 20×20 elements and two levels of refinement

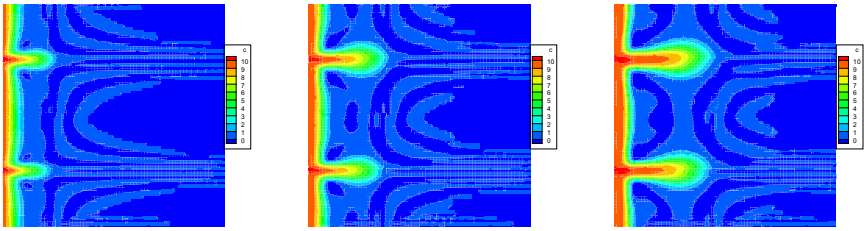

(a) c_{f_h} at $T = 20$, uniform mesh **(b)** c_{f_h} at $T = 35$, uniform mesh **(c)** c_{f_h} at $T = 50$, uniform mesh

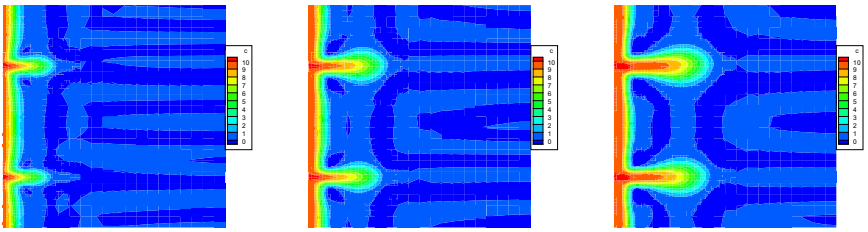

(d) c_{f_h} at $T = 20$, adaptive mesh **(e)** c_{f_h} at $T = 35$, adaptive mesh **(f)** c_{f_h} at $T = 50$, adaptive mesh

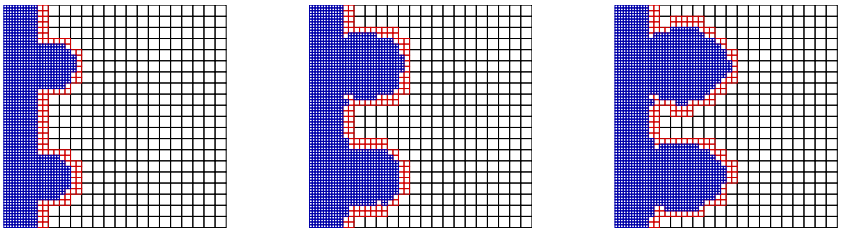

(g) $T = 20$, adaptive mesh **(h)** $T = 35$, adaptive mesh **(i)** $T = 50$, adaptive mesh

Fig. 2 Example 3: numerical concentration of acid with time evolution, the first line are results on a uniform mesh of 80×80 elements, the second line are results on an adaptive mesh, the third line are adaptive meshes with initial 20×20 elements and two levels of refinement

Example 6.2 A real wormhole propagation scenario in petroleum engineering is studied in this example. The parameters are taken as

$$\begin{aligned} &d_m = 10^{-8}, \quad \alpha_l = 0, \quad \alpha_t = 0, \quad K_0 = 10^{-9}\,\mathrm{m}^2, \quad T = 50\,\mathrm{s}, \\ &\alpha = 10\,\mathrm{kg/mol}, \quad k_c = 1\,\mathrm{m/s}, \quad k_s = 10\,\mathrm{m/s}, \\ &\mu = 10^{-2}\,\mathrm{Pa\,s}, \quad f_I = f_p = 0, \quad \rho = 1000, \quad \mathbf{g} = \mathbf{0}, \\ &a_0 = 2\,\mathrm{m}^{-1}, \quad \rho_s = 2500\,\mathrm{kg/m}^2, \quad \gamma = 0.01, \end{aligned} \tag{6.4}$$

The contour plots of concentration of acid, porosity of rock and velocity in x direction on adaptive mesh with time evolution are shown in Fig. 1. The adaptive meshes with two levels of refinement are used in this simulation, and the initial mesh is composed by 20×20 elements with equal size. Wormhole propagation is clearly shown from the figures on the adaptive mesh.

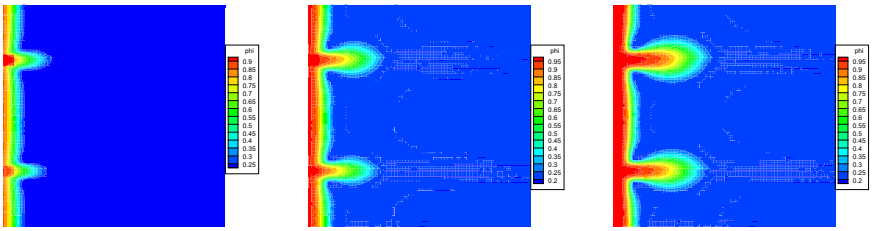

(a) ϕ_h at$T = 20$, uniform mesh **(b)** ϕ_h at$T = 35$, uniform mesh **(c)** ϕ_h at$T = 50$, uniform mesh

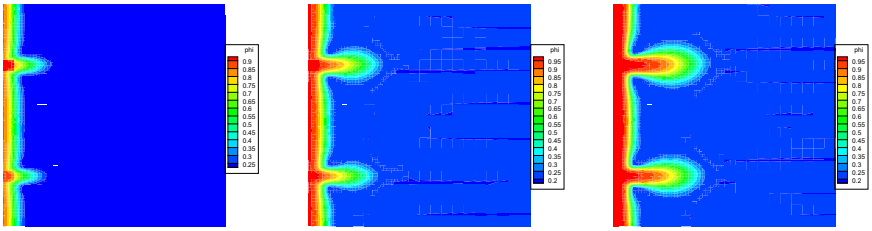

(d) ϕ_h at$T = 20$, adaptive mesh **(e)** ϕ_h at$T = 35$, adaptive mesh **(f)** ϕ_h at$T = 50$, adaptive mesh

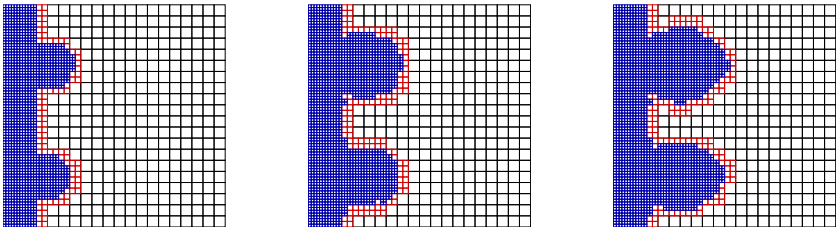

(g) $T = 20$, adaptive mesh **(h)** $T = 35$, adaptive mesh **(i)** $T = 50$, adaptive mesh

Fig. 3 Example 3: numerical porosity with time evolution, the first line are results on a uniform mesh of 80×80 elements, the second line are results on an adaptive mesh, the third line are adaptive meshes with initial 20×20 elements and two levels of refinement

Example 6.3 We simulate the real wormhole propagation scenario in Example 6.2 and take the same parameters except

$$\alpha_l = 10^{-3}, \quad \alpha_t = 10^{-4}. \tag{6.5}$$

The contour plots of concentration of acid, porosity of rock and velocity in x direction with time evolution are shown in Figs. 2, 3 and 4, respectively. Both a uniform mesh and an adaptive mesh are considered in the simulations, and the initial adaptive mesh is composed by 20×20 elements with two levels of refinement. From the results of Figs. 2, 3 and 4 we can observe that the numerical solutions are very similar on uniform mesh and on an adaptive mesh; and the wormhole propagations are shown clearly on both meshes. During the simulation of this example, the averaged number of elements on the adaptive mesh is 1865, compared with 6400 for the uniform mesh. We used Matlab to code up the example and ran it on a laptop. The simulation based on adaptive meshes took about 7 h, while that for

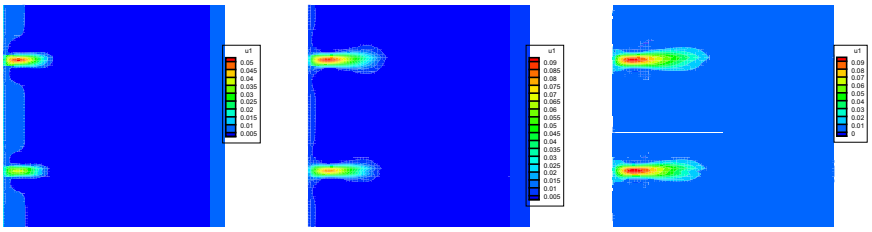

(a) u_{1h} at $T = 20$, uniform mesh **(b)** u_{1h} at $T = 35$, uniform mesh **(c)** u_{1h} at $T = 50$, uniform mesh

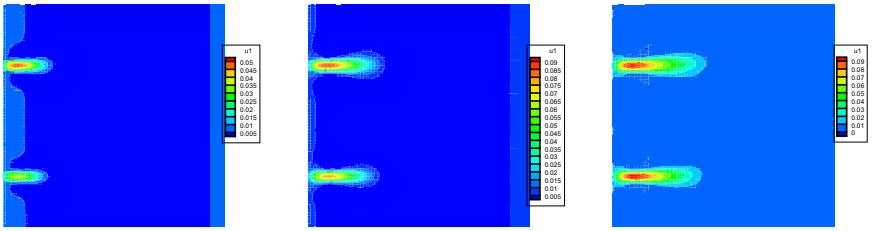

(d) u_{1h} at $T = 20$, adaptive mesh **(e)** u_{1h} at $T = 35$, adaptive mesh **(f)** u_{1h} at $T = 50$, adaptive mesh

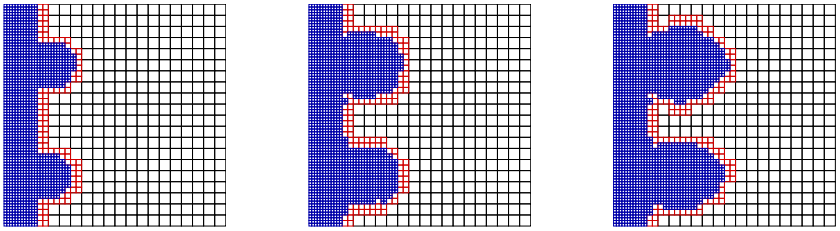

(g) $T = 20$, adaptive mesh **(h)** $T = 35$, adaptive mesh **(i)** $T = 50$, adaptive mesh

Fig. 4 Example 3: numerical velocity in x direction with time evolution, the first line are results on a uniform mesh of 80×80 elements, the second line are results on an adaptive mesh, the third line are adaptive meshes with initial 20×20 elements and two levels of refinement

uniform mesh may take 41 h until the final time $T = 50$ has been reached. We will consider further optimization and parallel technique in the future.

7 Concluding Remarks

In this paper, we studied the compressible wormhole prorogation, and optimal convergence rates were derived. Numerical experiments verified the theoretical analysis. Wormhole propagation was shown in the numerical simulations on both uniform and adaptive meshes.

Acknowledgements This work is supported by NSF Grant DMS-1818467, National Natural Science Foundation of China Grants 11801569 and 11571367, the Fundamental Research Funds for the Central Universities 18CX05003A, 18CX02021A and YJ201601010.

References

1. Ainsworth, M., Oden, J.T.: A posteriori error estimation in finite element analysis. Comput. Methods Appl. Mech. Eng. **142**, 1–88 (1997)
2. Bassi, F., Rebay, S.: A high-order accurate discontinuous finite element method for the numerical solution of the compressible Navier–Stokes equations. J. Comput. Phys. **131**, 267–279 (1997)
3. Braack, M., Prohl, A.: Stable discretization of a diffuse interface model for liquid–vapor flows with surface tension. ESAIM Math. Model. Numer. Anal. **47**, 401–420 (2013)
4. Berger, M.J., Colella, P.: Local adaptive mesh refinement for shock hydrodynamics. J. Comput. Phys. **82**, 64–84 (1989)
5. Castillo, P., Cockburn, B., Perugia, I., Schötzau, D.: Superconvergence of the local discontinuous Galerkin method for elliptic problems on Cartesian grids. SIAM J. Numer. Anal. **39**, 264–285 (2001)
6. Chuenjarern, N., Xu, Z., Yang, Y.: High-order bound-preserving discontinuous Galerkin methods for compressible miscible displacements in porous media on triangular meshes. J. Comput. Phys. **378**, 110–128 (2019)
7. Ciarlet, P.: The Finite Element Method for Elliptic Problem. SIAM, Philadelphia (1975)
8. Cockburn, B., Hou, S., Shu, C.W.: The Runge–Kutta local projection discontinuous Galerkin finite element method for conservation laws. IV: the multidimensional case. Math. Comput. **54**, 545–581 (1990)
9. Cockburn, B., Lin, S.Y., Shu, C.W.: TVB Runge–Kutta local projection discontinuous Galerkin finite element method for conservation laws. III: one-dimensional systems. J. Comput. Phys. **84**, 90–113 (1989)
10. Cockburn, B., Shu, C.W.: TVB Runge–Kutta local projection discontinuous Galerkin finite element method for conservation laws. II: general framework. Math. Comput. **52**, 411–435 (1989)
11. Cockburn, B., Shu, C.W.: The Runge–Kutta discontinuous Galerkin method for conservation laws. V: multidimensional systems. J. Comput. Phys. **141**, 199–224 (1998)
12. Cockburn, B., Shu, C.-W.: The local discontinuous Galerkin method for time-dependent convection–diffusion systems. SIAM J. Numer. Anal. **35**, 2440–2463 (1998)
13. Diehl, D.: Higher Order Schemes for Simulation of Compressible Liquid–Vapor Flows with Phase Change. Universität Freiburg, Freiburg im Breisgau (2007)
14. Fredd, C.N., Fogler, H.S.: Influence of transport and reaction on wormhole formation in porous media. Fluid Mech. Transp. Phenom. **44**, 1933–1949 (1998)
15. Gelfand, I.M.: Some questions of analysis and differential equations. Am. Math. Soc. Transl **26**, 201–219 (1963)
16. Golfier, F., Zarcone, C., Bazin, B., Lenormand, R., Lasseux, D., Quintard, M.: On the ability of a Darcy-scale model to capture wormhole formation during the dissolution of a porous medium. J. Fluid Mech. **457**, 213–254 (2002)
17. Guo, H., Tian, L., Xu, Z., Yang, Y., Qi, N.: High-order local discontinuous Galerkin method for simulating wormhole propagation. J. Comput. Appl. Math. **350**, 247–261 (2019)
18. Guo, H., Yang, Y.: Bound-preserving discontinuous Galerkin method for compressible miscible displacement problem in porous media. SIAM J. Sci. Comput. **39**, A1969–A1990 (2017)
19. Guo, H., Zhang, Q., Wang, J.: Error analysis of the semi-discrete local discontinuous Galerkin method for compressible miscible displacement problem in porous media. Appl. Math. Comput. **259**, 88–105 (2015)
20. Guo, H., Yu, F., Yang, Y.: Local discontinuous Galerkin method for incompressible miscible displacement problem in porous media. J. Sci. Comput. **71**, 615–633 (2017)
21. Hurd, A.E., Sattinger, D.H.: Questions of existence and uniqueness for hyperbolic equations with discontinuous coefficients. Trans. Am. Math. Soc. **132**, 159–174 (1968)
22. Jovanovic, V., Rohde, C.: Error estimates for finite volume approximations of classical solutions for nonlinear systems of hyperbolic balance laws. SIAM J. Numer. Anal. **43**, 2423–2449 (2006)
23. Kou, J., Sun, S., Wu, Y.: Mixed finite element-based fully conservative methods for simulating wormhole propagation. Comput. Methods Appl. Mech. Eng. **298**, 279–302 (2016)
24. Li, X., Rui, H.: Block-centered finite difference method for simulating compressible wormhole propagation. J. Sci. Comput. **74**, 1115–1145 (2018)
25. Li, X., Shu, C.-W., Yang, Y.: Local discontinuous Galerkin methods for Keller–Segel chemotaxis model. J. Sci. Comput. **73**, 943–967 (2017)
26. Liu, M., Zhang, S., Mou, J., Zhou, F.: Wormhole propagation behavior under reservoir condition in carbonate acidizing. Transp. Porous Media **96**, 203–220 (2013)
27. Liu, W., Cui, J.: A two-grid block-centered finite difference algorithm for nonlinear compressible Darcy–Forchheimer model in porous media. J. Sci. Comput. **74**, 1786–1815 (2018)
28. Mauran, S., Rigaud, L., Coudevylle, O.: Application of the Carman–Kozeny correlation to a highporosity and anisotropic consolidated medium: the compressed expanded natural graphite. Transp. Porous Media **43**, 355–376 (2001)

29. Ohlberger, M., Vovelle, J.: Error estimate for the approximation of nonlinear conservation laws on bounded domains by the finite volume method. Math. Comput. **75**, 113–150 (2006)
30. Oden, J.T., Wu, W., Ainsworth, M.: An a posteriori error estimate for finite element approximations of the Navier–Stokes equations. Comput. Methods Appl. Mech. Eng. **111**, 185–202 (1994)
31. Pan, H., Rui, H.: A mixed element method for Darcy–Forchheimer incompressible miscible displacement problem. Comput. Methods Appl. Mech. Eng. **264**, 1–11 (2013)
32. Pan, H., Rui, H.: Mixed element method for two-dimensional Darcy–Forchheimer model. J. Sci. Comput. **52**, 563–587 (2012)
33. Panga, M.K.R., Ziauddin, M.: Two-scale continuum model for simulation of wormholes in carbonate acidization. AIChE J. **51**, 3231–3248 (2005)
34. Qiu, J., Shu, C.W.: A comparison of troubled-cell indicators for Runge–Kutta discontinuous Galerkin methods using weighted essentially nonoscillatory limiters. SIAM J. Sci. Comput. **27**, 995–1013 (2005)
35. Reed, W.H., Hill, T.R.: Triangular mesh method for the neutron transport equation. Technical report LA-UR-73-479, Los Alamos Scientific Laboratory, Los Alamos, NM (1973)
36. Rui, H., Liu, W.: A two-grid block-centered finite difference method for Darcy–Forchheimer flow in porous media. SIAM J. Numer. Anal. **53**, 1941–1962 (2015)
37. Rui, H., Pan, H.: A block-centered finite difference method for slightly compressible Darcy–Forchheimer flow in porous media. J. Sci. Comput. **73**, 70–92 (2017)
38. Ruth, D., Ma, H.: On the derivation of the Forchheimer equation by means of the averaging theorem. Transp. Porous Media **7**, 255–264 (1992)
39. Shu, C.-W., Osher, S.: Efficient implementation of essentially non-oscillatory shock-capturing schemes. J. Comput. Phys. **77**, 439–471 (1988)
40. Smirnov, A.S., Fedorov, K.M., Shevelev, A.P.: Modeling the acidizing of a carbonate formation. Fluid Dyn. **45**, 779–786 (2010)
41. Szymczak, P., Ladd, A.J.C.: Wormhole formation in dissolving fractures. J. Gophys. Res. **114**, B06203 (2009)
42. Tian, L., Xu, Y., Kuerten, J.G.M., Van der Vegt, J.J.W.: An h-adaptive local discontinuous Galerkin method for the Navier–Stokes–Korteweg equations. J. Comput. Phys. **319**, 242–265 (2016)
43. Verfürth, R.: A posteriori error estimators for the Stokes equations. Numer. Math. **55**, 309–325 (1989)
44. Verfürth, R.: A review of a posteriori error estimation techniques for elasticity problems. Comput. Methods Appl. Mech. Eng. **176**, 419–440 (1999)
45. Vilsmeier, R., Hänel, D.: Adaptive methods on unstructured grids for Euler and Navier–Stokes equations. Comput. Fluids **22**, 485–499 (1993)
46. Wang, H., Shu, C.-W., Zhang, Q.: Stability and error estimates of local discontinuous Galerkin methods with implicit–explicit time-marching for advection–diffusion problems. SIAM J. Numer. Anal. **53**, 206–227 (2015)
47. Wang, H., Shu, C.-W., Zhang, Q.: Stability analysis and error estimates of local discontinuous Galerkin methods with implicit–explicit time-marching for nonlinear convection–diffusion problems. Appl. Math. Comput. **272**, 237–258 (2016)
48. Wang, H., Wang, S., Zhang, Q., Shu, C.-W.: Local discontinuous Galerkin methods with implicit–explicit time marching for multi-dimensional convection–diffusion problems. ESAIM: M2AN **50**, 1083–1105 (2016)
49. Wu, Y., Salama, A., Sun, S.: Parallel simulation of wormhole propagation with the Darcy–Brinkman–Forchheimer framework. Comput. Geotech. **69**, 564–577 (2015)
50. Xu, W., Liang, D., Rui, H.: A multipoint flux mixed finite element method for the compressible Darcy–Forchheimer models. Appl. Math. Comput. **315**, 259–277 (2017)
51. Xu, Y., Shu, C.-W.: Local discontinuous Galerkin methods for nonlinear Schrödinger equations. J. Comput. Phys. **205**, 72–97 (2005)
52. Xu, Y., Shu, C.-W.: Error estimates of the semi-discrete local discontinuous Galerkin method for nonlinear convection–diffusion and KdV equations. Comput. Methods Appl. Mech. Eng. **196**, 3805–3822 (2007)
53. Xu, Z., Yang, Y., Guo, H.: High-order bound-preserving discontinuous Galerkin methods for wormhole propagation on triangular meshes. J. Comput. Phys. **390**, 323–341 (2019)
54. Yan, J., Shu, C.-W.: Local discontinuous Galerkin methods for partial differential equations with higher order derivatives. J. Sci. Comput. **17**, 27–47 (2002)
55. Yan, J., Shu, C.-W.: A local discontinuous Galerkin method for KdV type equations. SIAM J. Numer. Anal. **40**, 769–791 (2002)
56. Yang, Y., Shu, C.-W.: Analysis of optimal superconvergence of local discontinuous Galerkin method for one-dimensional linear parabolic equations. J. Comput. Math. **33**, 323–340 (2015)
57. Yu, F., Guo, H., Chuenjarern, N., Yang, Y.: Conservative local discontinuous Galerkin method for compressible miscible displacements in porous media. J. Sci. Comput. **73**, 1249–1275 (2017)

58. Zhao, C., Hobbs, B.E., Hornb, P., Ord, A., Peng, S., Liu, L.: Theoretical and numerical analyses of chemical-dissolution front instability in fluid-saturated porous rocks. Int. J. Numer. Anal. Methods Geomech. **32**, 1107–1130 (2008)
59. Zhao, Q., Rui, H., Liu, W.: Cell-centered finite difference method for the one-dimensional Forchheimer laws. Bull. Malays. Math. Sci. Soc. **40**, 545–564 (2017)
60. Zhu, H., Qiu, J.: Adaptive Runge–Kutta discontinuous Galerkin methods using different indicators: one-dimensional case. J. Comput. Phys. **228**, 6957–6976 (2009)
61. Zhu, H., Qiu, J.: An h-adaptive RKDG method with troubled-cell indicator for two-dimensional hyperbolic conservation laws. Adv. Comput. Math. **39**, 445–463 (2013)